

Polarization and Holography Recording in Real- and k -Space Based on Dielectric Metasurface

Ruizhe Zhao, Xiaofei Xiao, Guangzhou Geng, Xin Li, Junjie Li, Xiaowei Li, Yongtian Wang,* and Lingling Huang*

The diverse design freedom and mechanisms of metasurfaces motivate the manipulation of polarization in an ultrashort distance with subwavelength resolution and make metasurfaces outperform conventional polarization optical elements. However, in order to enhance the information capability and encryption security of metasurface holograms, polarization manipulation together with multiplexing technologies are still highly desired. Here, a birefringent dielectric metasurface with the capability of encoding a grayscale image in real-space based on Malus's law by utilizing the inhomogeneous polarization distribution and realizing the reconstruction of a vectorial holographic image in k -space with the help of the phase profiles of different polarization components of output light is demonstrated. This novel functionality is realized by exploiting the manipulation of polarization and phase of output light simultaneously offered by the dielectric metasurface. The proposed method may enhance the information capability and security level of applications such as the anticounterfeiting and encryption.

subwavelength resolution and become a potential substitute for the traditional bulky optical elements.^[1–4] The diverse design freedoms offered by meta-atoms and different working mechanisms of metasurfaces motivate the manipulation of the amplitude,^[5,6] phase,^[7–9] polarization,^[10–12] frequency,^[13,14] or simultaneously multiple parameters^[15–18] of output light, leading to various novel applications such as metalens,^[19–21] nonlinear optics,^[22–24] holography,^[25–29] color printing,^[30,31] as well as optical anticounterfeiting and encryption.^[32,33]

Holography based on metasurfaces are widely used to encode the desired images in the predefined positions due to their ability to restore and reconstruct the full wave information of object targets.^[34–36] In order to enhance the information capability of metasurface holograms, suitable multiplexing methods are very necessary for encoding multiple images within a single metasurface and in favor of applications such as encryption, anticounterfeiting, information storage, and so on. As the fundamental properties of light, the frequency,^[37,38] polarization,^[39–42] incident angle,^[43,44] orbital angular momentum,^[45,46] and the incoming direction of the incident light^[47,48] are all the optical channels that can be utilized to achieve multiplexing and many intriguing schemes are demonstrated in these years. Recently, some methods are proposed to achieve encoding different images in real- and k -space simultaneously by modulating spectral and spatial responses at subwavelength scale or exploiting the multiple dimensional modulation of output light based on carefully designed metasurfaces.^[49–51] By integrating a color filter and a phase plate into one pixel, an optical security device was demonstrated with the capability of encoding a color image under white light, but revealed three different hidden holographic projections when illuminated by red, green, and blue lasers.^[49] Meanwhile, optimized amorphous silicon dimers and nanofins^[50] or Fabry–Pérot cavity-based color filter microarray^[51] can also be adopted to realize integrating color printing together with holography in order to encode a color image and a holographic image in real-space and k -space, respectively. Furthermore, the phase information of transmitted light in real-space is another design freedom we can utilize. The phase pattern encoded in different polarization channels at both two spaces have been demonstrated, where the near field phase profile can be extracted using quadriwave lateral shearing interferometry technique.^[52] In the

1. Introduction


Metasurfaces composed of plasmonic or dielectric nanoantennas have attracted enormous interest due to their ability to arbitrarily tailor the wavefront in ultrashort distance with

R. Zhao, Prof. X. Li, Prof. Y. Wang, Prof. L. Huang
Beijing Engineering Research Center of Mixed Reality
and Advanced Display
School of Optics and Photonics
Beijing Institute of Technology
Beijing 100081, China
E-mail: wyt@bit.edu.cn; huanglingling@bit.edu.cn

Dr. X. Xiao
Department of Physics
Imperial College London
London SW7 2AZ, UK

Prof. G. Geng, Prof. J. Li
Beijing National Laboratory for Condensed Matter Physics
Institute of Physics
Chinese Academy of Sciences
Beijing 100191, China

Prof. X. Li
Laser Micro/Nano-Fabrication Laboratory
School of Mechanical Engineering
Beijing Institute of Technology
Beijing 100081, China

 The ORCID identification number(s) for the author(s) of this article can be found under <https://doi.org/10.1002/adfm.202100406>.

DOI: 10.1002/adfm.202100406

nonlinear optical regime, a plasmonic metasurface composed of diatomic meta-molecules was proposed to encode an intensity image in the real-space based on the interference between the second harmonic generation waves in a meta-molecule. And a holographic image was reconstructed in the k -space due to the spin-controlled geometric phase.^[53] Nevertheless, the polarization distributions of the reconstructed holographic images using the mentioned methods are all homogeneous, which make them more easy to be detected and the polarization of output light can also be utilized to realize more complicated functionalities.

Here, we demonstrate two types of birefringent dielectric metasurfaces with the capabilities of encoding a binary or four-level grayscale image in real-space based on Malus's law and achieving the reconstruction of vectorial holographic images in k -space by exploiting the phase profiles of different polarization components. The encoded grayscale images can only be observed with the assistance of a linear polarizer as an analyzer by selecting the correct polarization component. Meanwhile, various vectorial features of the reconstructed vectorial holographic images in k -space can be acquired. Such novel functionality is realized due to the complete control of the phase and polarization of output light, which is offered by the birefringent metasurface. Meanwhile, the birefringent metasurface is designed by analyzing the eigenvalue and eigenvector of desired Jones matrix at each pixel. The proposed scheme can increase the information capability of metasurface hologram by encoding different images in real- and k -space, respectively. Meanwhile, it also provides a platform for realizing multidimensional optical information encryption and anticounterfeiting with enhanced security level due to the vectorial feature of the reconstructed images.

2. Results

A schematic illustration of the proposed birefringent dielectric metasurface for encoding different images in real-space and k -space is shown in **Figure 1**. When an incident light with a linear polarization at 45° illuminating on the designed metasurface, the polarization and phase of output light can be tailored pixel by pixel with nearly uniform amplitude distribution. Without the assistance of a linear polarizer as an analyzer, no distinct images can be detected in real-space. In contrast, when an analyzer is inserted behind the metasurface with its transmission axis in horizontal or vertical direction, two complementary QR codes can be clearly observed, due to the inhomogeneous polarization distribution based on Malus's law. Furthermore, the phase profiles of different polarization components of the output light can yield the reconstruction of a vectorial holographic image (a butterfly with inhomogeneous polarization distribution) in k -space. And the vectorial feature of the reconstructed holographic image can be acquired by the polarization analyses.

For the purpose of encoding a grayscale image in real-space and a vectorial holographic image in k -space, we establish a modified GS algorithm and its flowchart is shown in **Figure 2**. A QR code with the intensity distribution A_1 is chosen as the encoded grayscale image and can be detected by rotating the transmission axis of the analyzer to horizontal direction. The

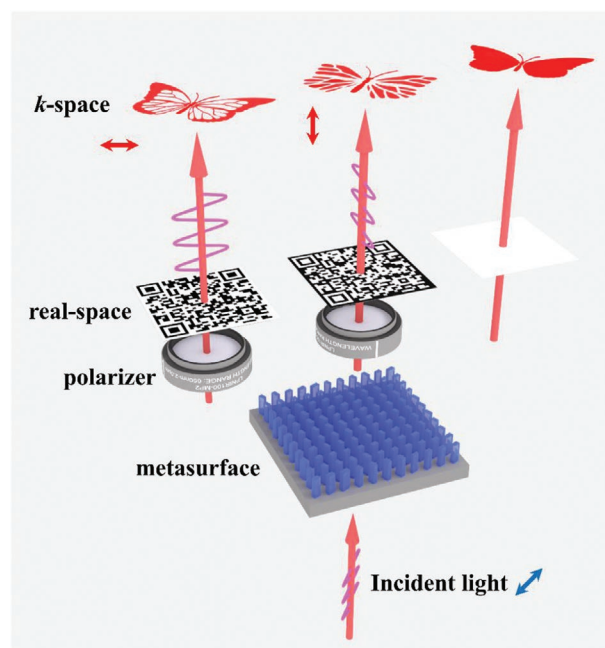


Figure 1. Schematic illustration of a dielectric metasurface with the capabilities of encoding a QR code in real-space and a vectorial holographic image in k -space, respectively. The blue and red arrows indicate the polarization of incident light and the transmission axis of polarizer placed behind the metasurface sample.

corresponding polarization distribution p of output light can be determined by the intensity distribution A_1 of the QR code based on Malus's law. The white and black areas of the QR code represent the x - and y -linear polarization state, respectively. Meanwhile, the intensity distribution of its complementary one is indicated by A_2 . The propagation processes between the hologram plane and the object plane are constructed by the Fourier transform and inverse Fourier transform (IFFT). In our algorithm, the amplitude replacement at the hologram plane is achieved by the amplitude distribution A_1 or A_2 , which is different from the traditional GS algorithm that exploits the normalized amplitude to replace the calculated amplitude distribution by IFFT. Meanwhile, two parts of a butterfly image which correspond to the x - and y -linearly polarized polarization components of the vectorial holographic image are utilized as the target objects in the iterative processes. After a sufficient number of iterations, we obtain the optimized phase profiles φ_1 and φ_2 . And the final hologram φ_h is then calculated by:

$$\varphi_h = \arg(A_1 \exp(i\varphi_1) + A_2 \exp(i\varphi_2)) \quad (1)$$

Our proposed dielectric metasurface is composed of α -Si nanofins on top of a quartz substrate as shown in **Figure 3a**. The high-index dielectric nanofin can be considered as a tiny waveguide with different effective refractive index (n_{eff}) along its long and short axis, resulting in the birefringence phenomenon.^[54] Especially, the n_{eff} can be tailored by adjusting the length, L , and width, W , of the nanofin, and arbitrary phase delay can be imposed between two orthogonal polarization components of the input light, allowing full control of the polarization. The relation between the output and input light is

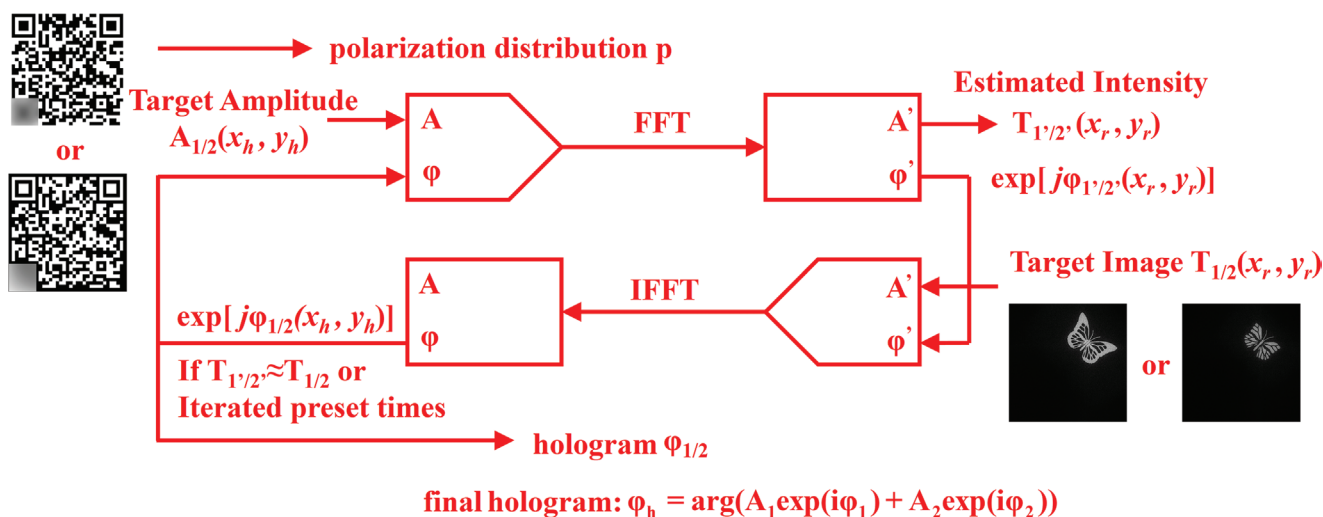


Figure 2. The flow chart of the modified Gerchberg–Saxton algorithm for generating the required phase distribution. The polarization distribution, p , is determined by the QR code where the white areas indicate x-linear polarization and the black areas represent y-linear polarization. The amplitude distributions of two complementary QR codes are indicated by A_1 and A_2 , respectively. And the T_1 and T_2 represent two target images. The “FFT” and “IFFT” represent the Fourier transform and inverse Fourier transform for investigating the propagation processes between the hologram plane and the object plane.

commonly linked through the Jones matrix method and can be expressed in linear polarization basis:

$$\begin{bmatrix} E_x^{out} \\ E_y^{out} \end{bmatrix} = \begin{bmatrix} t_{xx} & t_{xy} \\ t_{yx} & t_{yy} \end{bmatrix} \begin{bmatrix} E_x^{in} \\ E_y^{in} \end{bmatrix} \quad (2)$$

where the subscript i and j of the transmission coefficients t_{ij} indicate the output and input polarization components,

respectively. For a desired symmetric Jones matrix T with nearly unitary transmitted amplitude (satisfying the condition of unitary matrix $T^\dagger T = T T^\dagger = I$), it can be realized by a birefringent metasurface if the polarization-dependent phase shift (ϕ_x, ϕ_y) and the orientation angle, θ , can be chosen freely:^[16]

$$T = R(\theta) \begin{bmatrix} e^{i\phi_x} & 0 \\ 0 & e^{i\phi_y} \end{bmatrix} R(-\theta) \quad (3)$$

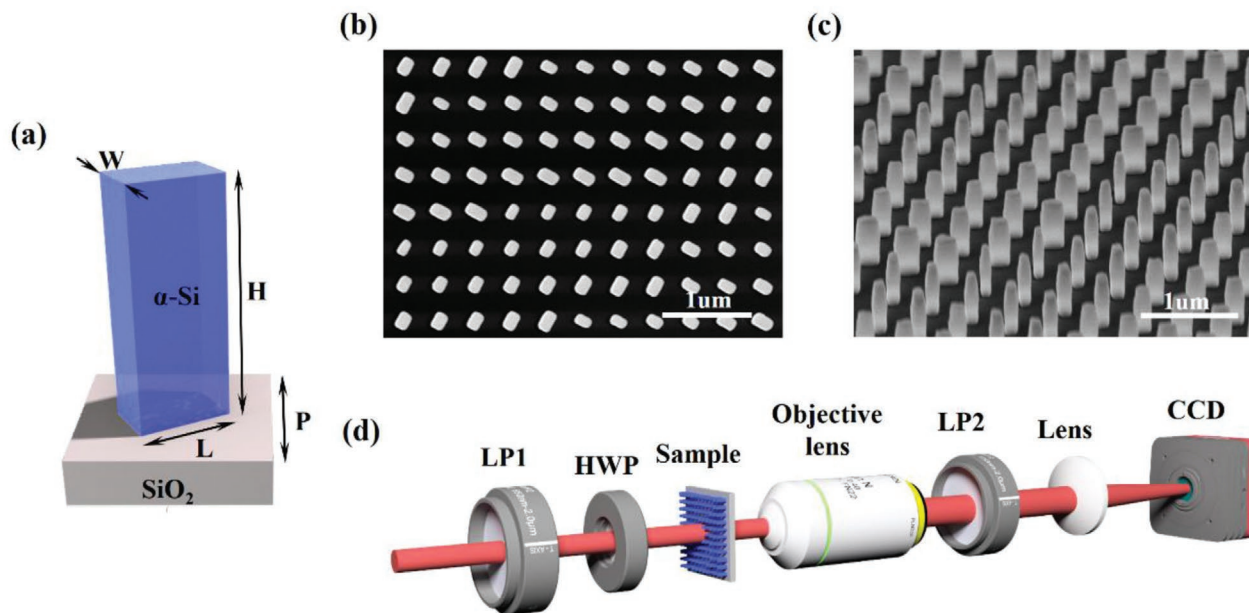


Figure 3. a) Schematic illustration of an amorphous silicon nanofin positioned on a fused quartz substrate. b,c) The scanning electron microscopy images of our fabricated metasurface sample 1 in top and side view. The metasurface is composed of 1000×1000 α -Si nanofins with different cross sections and orientation angles. d) The experimental setup for capturing the encoded images in real-space and k -space. The linear polarizer LP1 and half-wave plate HWP are used to control the polarization of incident light. The linear polarizer LP2 is used to distinguish the x- and y-polarized component of output light. The fabricated metasurface sample is placed on the focal plane of an objective lens ($50\times/0.8$). The holographic images in k -space are observed at the focal plane of a lens ($f = 100$ mm) and captured by a CCD camera. And the QR codes are obtained when we move the CCD close to the lens.

The $R(\theta)$ in Equation (3) indicates that the rotation matrix and the diagonal elements can be achieved by choosing suitable sizes of the meta-atoms. By integrating the geometric phase with propagation phase, the phase and polarization of the output light can be arbitrarily controlled simultaneously. In addition, independent phase profiles can be imparted on any set of orthogonal polarization states which breaks the limitation of traditional geometric phase metasurfaces that can only achieve conjugate phase modulation when flipping the helicity of incident circularly polarized light.^[39,40]

For achieving the desired phase shifts (ϕ_x, ϕ_y) with high efficiency and eliminating undesired orders of diffraction, the period, P , and height, H , of each α -Si nanofin are chosen as 400 and 600 nm, respectively. A 2D parameter optimization is carried out by using the rigorous coupled wave analysis method and the length, L , and width, W , of the nanofin are both swept in the range of 60–280 nm with an interval of 5 nm. The working wavelength is fixed at 800 nm and the corresponding refractive index of amorphous silicon and substrate are set as $n_{\text{Si}} = 3.802$ and $n_{\text{sub}} = 1.5$ in the simulation. The simulated amplitude ($\text{abs}(t_{xx})$ and $\text{abs}(t_{yy})$) and phase (ϕ_x and ϕ_y) of transmission coefficients t_{xx} and t_{yy} are shown in Figure S1a–d, Supporting Information. We can observe that the $\text{abs}(t_{xx})$ and $\text{abs}(t_{yy})$ of most sizes of nanofins are over 90% which can be utilized to achieve desired Jones matrix. Meanwhile, the desired phase shifts (ϕ_x, ϕ_y) and the orientation angle, θ , of each α -Si nanofin of our demonstrated metasurface are calculated according to the Jones vector of the incident light $\sqrt{2}/2[1, 1]^T$, polarization distribution p and the phase profile ϕ_h through Equations (2) and (3). And the size of each nanofin is determined by the calculated phase shifts (ϕ_x, ϕ_y) as well as the phase of transmission coefficients t_{xx} and t_{yy} . Before fabricating the designed metasurfaces, we simulated the performances of the metasurfaces that are composed of 80×80 unit cells (size: $32 \times 32 \mu\text{m}^2$) under 45° linearly polarized light and LCP light based on the finite difference time domain method. The simulation details can be found in Section B, Supporting Information.

In order to confirm the theoretical results, we fabricated two types of dielectric metasurfaces named sample 1 and sample 2 on top of a fused quartz substrate by electron beam lithography followed a plasma etching process (detail information is provided in Supporting Information). Two scanning electron microscopy images of sample 1 with a top view and side view are shown in Figure 3b,c. The fabricated metasurface composed of 1000×1000 pixels with the period $P = 400$ nm. Meanwhile, the length, L , and width, W , of each nanofin are in the range of 60–280 nm with different orientation angle θ ($\theta = 22.5^\circ$ or 67.5°). The selected nanofins with different sizes from the simulated results can be considered as almost ideal half-wave plates with different ϕ_x which can rotate the incident 45° linearly polarized light to x - or y -direction and offer different phase delay simultaneously. We utilize the setup shown in Figure 3d to capture the encoded images in real-space and k -space in the experiment. A linear polarizer LP1 and a half-wave plate HWP are put in front of the metasurface for manipulating the polarization angle of the input linearly polarized light. And our metasurface sample is placed at the working distance of an objective lens ($\times 50/\text{NA} = 0.8$). The numerical

aperture of the objective lens is chosen carefully for collecting all the diffraction light from the sample and reconstructing the holographic images. Another linear polarizer LP2 is used as an analyzer to distinguish the polarization of output light. The QR codes encoded in real-space are captured by a charge coupled device camera (CCD) behind the LP2. While, the vectorial holographic image in k -space is obtained when we move the CCD to the back focal plane of a lens.

The simulated and experimental results of the encoded images in real-space and k -space are shown in Figure 4. When the 45° linearly polarized light with the wavelength of 800 nm is illuminated on the fabricated metasurface, uniform amplitude distribution is obtained in real-space as shown in Figure 4g. While, after inserting a linear polarizer LP2 as an analyzer behind the metasurface, two complementary QR codes are clearly observed as depicted in Figure 4h,i due to the inhomogeneous polarization distribution based on Malus's law. And a flower picture can be acquired by scanning the captured QR codes. In the k -space, a vectorial holographic image of a butterfly is reconstructed at the back focal plane of a lens as shown in Figure 4j. The x - and y -linearly polarized component of the holographic image can be selected and observed clearly by rotating the transmission axis of the analyzer, as shown in Figure 4k,l. In the experiment, the measured transmission efficiency of the fabricated metasurface is 76.93%. The diffraction efficiency which is defined as the power of the reconstruct holographic images (observed without LP2) divided by the power of the incident light is 33.73%. In addition, our fabricated metasurface represents high performance by changing the incident wavelength from 700 to 780 nm. The corresponding experimental results and the explanation for the broadband properties are provided in the Supporting Information.

Furthermore, we demonstrate that our proposed method can achieve more complicated functionality. We choose a four-level grayscale polarized pattern (gray level = 0.25, 0.5, 0.75, 1) represented in Figure S3, Supporting Information, as the image that is encoded in real-space when the transmission axes of the linear polarizer LP1 and LP2 are rotated to the vertical and horizontal direction, respectively. The polarization states of the four different areas of sample 2 are all linearly polarized but with different polarization angle θ_p ($\theta_p = 0^\circ, 30^\circ, 135^\circ$, and 60°). The detected intensity of each area can be calculated using Equation (4), where I_0 is the intensity of incident light and θ_0 represents the direction of the transmission axis of LP2.

$$I = I_0 \cos^2(\theta_p - \theta_0) \quad (4)$$

In the process of designing sample 2, we set $I_0 = 1$, $\theta_0 = 0^\circ$ and I is represented by the gray level of different areas in the four-level grayscale polarized pattern. By utilizing the modified GS algorithm, we generate the final phase profile ϕ_h and encode it into sample 2. Meanwhile, the phase profiles of different polarization components yield the reconstruction of a vectorial holographic image composed of four letters (A, B, C, and D) in k -space. In order to verify the polarization states of the encoded grayscale image and the holographic image, we rotate

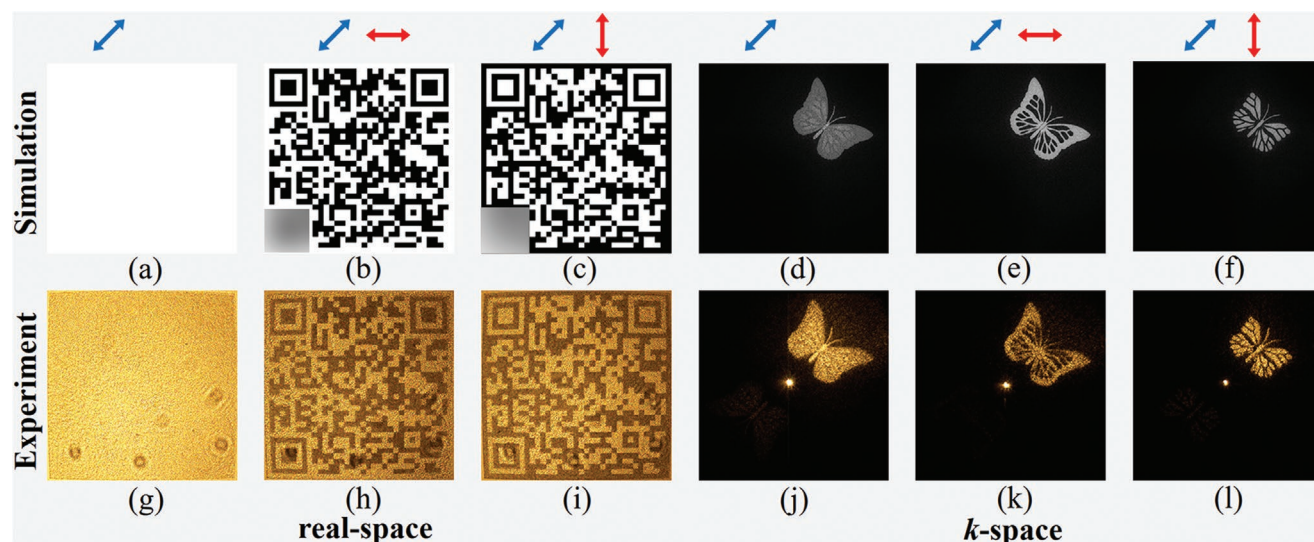


Figure 4. a–l) Simulated and experimental results of our fabricated metasurface sample 1 with the capability of encoding a QR code and a vectorial holographic image in real- and k -space when the wavelength of incident light is 800 nm. The blue and red arrows indicate the polarization of input and output light, respectively.

the transmission axis of the analyzer LP2 to different directions ($\theta_0 = 90^\circ, 120^\circ, 45^\circ$, and 150°) and sequentially observe the corresponding areas of sample 2 in real-space and the letters in k -space are extinct, as illustrated in **Figure 5**. Meanwhile, the intensities of different captured letters shown in Figure 5q–t agree well with the corresponding simulated results that calculated using Equation (4) by changing θ_0 to different values. While, in Figure 5f we can still observe the blurred outline of four-level grayscale polarized pattern which may be caused by the abrupt change of orientations of the nanofins between different areas and unavoidable fabrication deviation of the sample. In the experiment, the measured transmission efficiency and diffraction efficiency of sample 2 are 60.10% and 28.98%, respectively. The zero order is mainly caused by the incident light that transmits directly through the sample. And its intensity can be calculated based on Malus's law by considering the polarization of incident light as well as the direction of the transmission axis of the linear polarizer LP2. In Figure 5q–t, the transmission axis of the analyzer LP2 is rotated to $90^\circ, 120^\circ, 45^\circ$, and 150° successively. Therefore, the calculated ratio of the intensities of the zero order in Figure 5q–t is 1:0.75:0.5:0.25 and the zero order in Figure 5t is weakest.

The types of the polarization states of the encoded reconstructed vectorial holographic images are determined by the number of the segments that we divided in the metasurface. In each segment, the corresponding array of the Si nanofins can convert the polarization of incident light into specific polarization state based on the gray level of the encoded grayscale pattern in real-space. Meanwhile, the phase distribution of the output light from each segment can also be controlled arbitrarily and contribute to the reconstruction of the corresponding part of the vectorial holographic image. Note that, the areas of each divided segment need to be relatively uniform in order to guarantee the uniform intensities of different parts of the holographic image. Furthermore, such simultaneously

polarization and phase modulation can also achieve spatially variant vectorial holography.

3. Conclusion

With the development of nanofabrication technologies,^[55,56] metasurfaces have attracted enormous interests due to their ability to manipulate the wavefront of output light arbitrarily with subwavelength resolution from visible region to THz region.^[57,58] These distinct advantages have made metasurface holography represent superior performances over traditional holography based on the spatial light modulator in certain areas such as the resolution of reconstructed images, space-bandwidth, and field-of-view. Therefore, metasurfaces have been considered as promising devices for achieving applications including display, imaging, anticounterfeiting, and encryption.^[34]

In summary, we have demonstrated a birefringent dielectric metasurface with the capability of encoding a polarized grayscale image with high contrast in real-space based on Malus's law. While the phase profiles of different polarization components of output light can be utilized to reconstruct distinct vectorial holography with inhomogeneous polarization distribution in k -space, which are different from previous proposed works that reconstruct holographic images with homogeneous polarization distribution. Such method is realized by controlling the phase and polarization of output light simultaneously. The vectorial feature of the holographic images we obtained can increase the security level. Furthermore, by integrating this scheme with deep learning method or other algorithms for computing the holograms, the number of the images that encoded within one single metasurfaces in real- and k -space may be further increased, and the ultimate vectorial holography for mimicking the natural polarization states of scattering

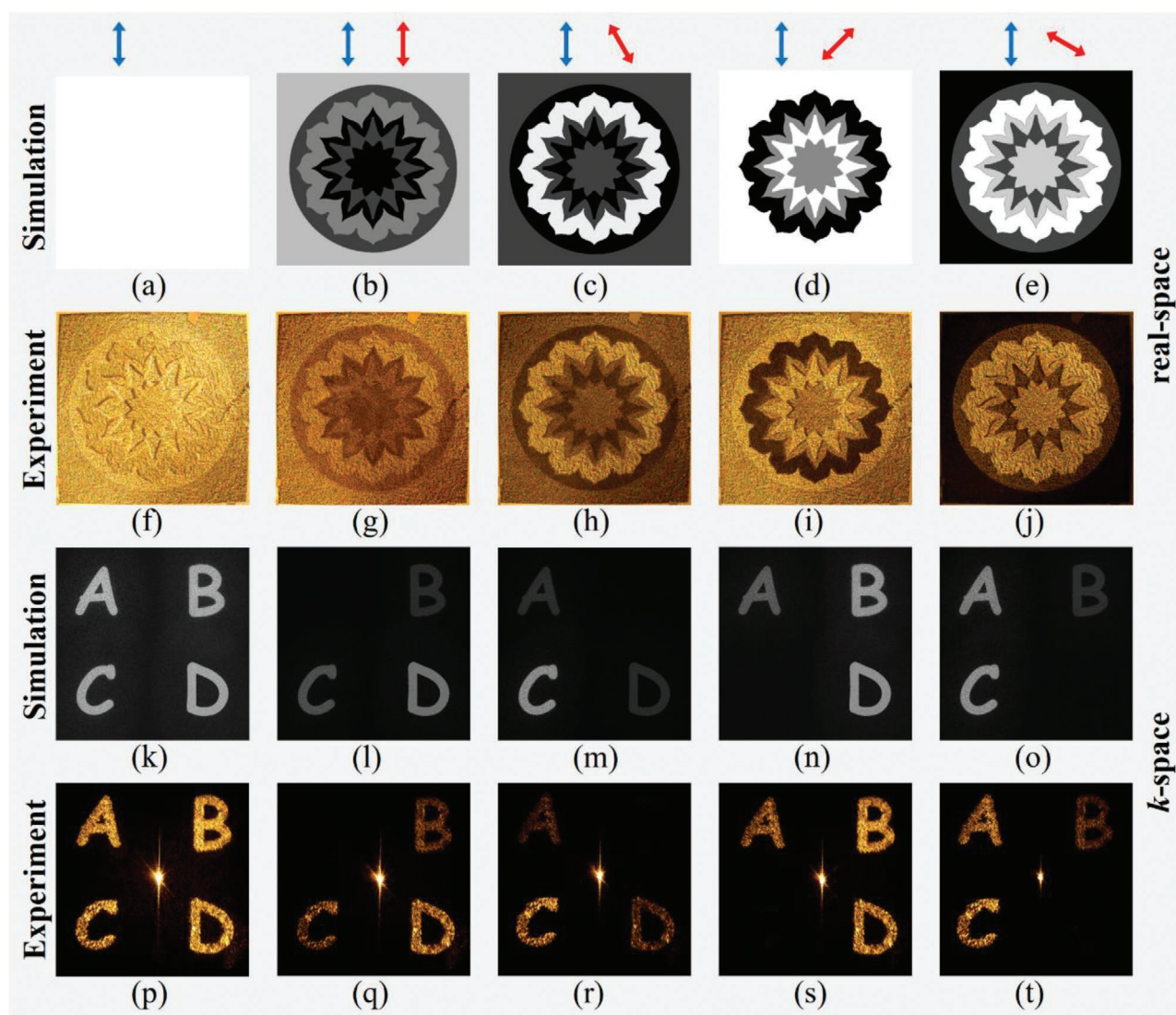


Figure 5. a–j) Simulated and experimental results of the four-level grayscale polarized image encoded in sample 2 in real-space. k–t) Simulated and experimental results of the reconstructed holographic images consist of the letters A, B, C, and D in k-space. The incident wavelength is 800 nm. The blue and red arrows indicate the polarization of input and output light, respectively. The polarization states of the four different areas of sample 2 and the reconstructed holographic images A, B, C, and D are all linearly polarized but with different polarization angle θ_p ($\theta_p = 0^\circ, 30^\circ, 135^\circ$, and 60°). When we rotate the transmitted axis of the analyzer LP2 to $90^\circ, 120^\circ, 45^\circ$, and 150° successively, correct extinction phenomenon can be observed which verify the polarization state of the images encoded in real- and k-space.

objects can be achieved. Such scheme may provide a new route to information storage, anticounterfeiting, and encryption.

Scientist Program (BJJWZYJH01201910007022), National Natural Science Foundation of China (No. 61775019, No. 92050117, No. 61861136010) program, and the Fok Ying-Tong Education Foundation of China (No. 161009).

Supporting Information

Supporting Information is available from the Wiley Online Library or from the author.

Conflict of Interest

The authors declare no conflict of interest.

Acknowledgements

The authors acknowledge the funding provided by the National Key R&D Program of China (No. 2017YFB1002900), Beijing Outstanding Young

Author Contributions

L.H. and X.X. proposed the idea; R.Z. and X.X. conducted pattern designs and numerical simulations; R.Z. conducted the hologram generations;

G.G. and J.L. fabricated the samples; R.Z. and X.L. performed the measurements; and R.Z., X.X., and L.H. prepared the manuscript. L.H. and Y.W. supervised the overall projects. All the authors analyzed the data and discussed the results.

Data Availability Statement

The data that support the findings of this study are available from the corresponding author upon reasonable request.

Keywords

holography, image encoding, metasurfaces

Received: January 14, 2021

Revised: March 24, 2021

Published online:

- [1] N. Yu, F. Capasso, *Nat. Mater.* **2014**, *13*, 139.
- [2] A. V. Kildishev, A. Boltasseva, V. M. Shalae, *Science* **2013**, *339*, 1232009.
- [3] P. Genevet, F. Capasso, F. Aieta, M. Khorasaninejad, R. Devlin, *Optica* **2017**, *4*, 139.
- [4] X. Fu, T. J. Cui, *Prog. Quantum Electron.* **2019**, *67*, 100223.
- [5] K. Huang, H. Liu, F. J. Garcia-Vidal, M. H. Hong, B. Luk'yanchuk, J. H. Teng, C. W. Qiu, *Nat. Commun.* **2015**, *6*, 7059.
- [6] J. Li, Y. Zhang, J. Li, X. Yan, L. Liang, Z. Zhang, J. Huang, J. Li, Y. Yang, J. Yao, *Nanoscale* **2019**, *11*, 5746.
- [7] N. Yu, P. Genevet, M. A. Kats, F. Aieta, J. P. Tetienne, F. Capasso, Z. Gaburro, *Science* **2011**, *334*, 333.
- [8] S. Sun, Q. He, S. Xiao, Q. Xu, X. Li, L. Zhou, *Nat. Mater.* **2012**, *11*, 426.
- [9] L. Huang, X. Chen, H. Muhlenbernd, G. Li, B. Bai, Q. Tan, G. Jin, T. Zentgraf, S. Zhang, *Nano Lett.* **2012**, *12*, 5750.
- [10] S. Kruk, B. Hopkins, I. I. Kravchenko, A. Miroshnichenko, D. N. Neshev, Y. S. Kivshar, *APL Photonics* **2016**, *1*, 030801.
- [11] T. Li, L. Huang, J. Liu, Y. Wang, T. Zentgraf, *Opt. Express* **2017**, *25*, 4216.
- [12] K. Guo, H. Xu, Z. Peng, X. Liu, Z. Guo, *IEEE Sens. J.* **2019**, *19*, 3654.
- [13] G. Li, S. Chen, N. Pholchai, B. Reineke, P. W. H. Wong, E. Y. B. Pun, K. W. Cheah, T. Zentgraf, S. Zhang, *Nat. Mater.* **2015**, *14*, 607.
- [14] W. Ye, F. Zeuner, X. Li, B. Reineke, S. He, C. Qiu, J. Liu, Y. Wang, S. Zhang, T. Zentgraf, *Nat. Commun.* **2016**, *7*, 11930.
- [15] G. Y. Lee, G. Yoon, S. Y. Lee, H. Yun, J. Cho, K. Lee, H. Kim, J. Rho, B. Lee, *Nanoscale* **2018**, *10*, 4237.
- [16] A. Arbabi, Y. Horie, M. Bagheri, A. Faraon, *Nat. Nanotechnol.* **2015**, *10*, 937.
- [17] Z. Deng, M. Jin, X. Ye, S. Wang, T. Shi, J. Deng, N. Mao, Y. Cao, B. Guan, A. Alu, G. Li, X. Li, *Adv. Funct. Mater.* **2020**, *30*, 1910610.
- [18] Y. Bao, J. Ni, C. W. Qiu, *Adv. Mater.* **2020**, *32*, 1905659.
- [19] M. Khorasaninejad, W. T. Chen, R. C. Devlin, J. Oh, A. Y. Zhu, F. Capasso, *Science* **2016**, *352*, 1190.
- [20] W. T. Chen, A. Y. Zhu, V. Sanjeev, M. Khorasaninejad, Z. J. Shi, E. Lee, F. Capasso, *Nat. Nanotechnol.* **2018**, *13*, 220.
- [21] S. Wang, P. C. Wu, V. C. Su, Y. C. Lai, M. K. Chen, H. Y. Kuo, B. H. Chen, Y. H. Chen, T. T. Huang, J. H. Wang, R. M. Lin, C. H. Kuan, T. Li, Z. Wang, S. Zhu, D. P. Tsai, *Nat. Nanotechnol.* **2018**, *13*, 227.
- [22] L. Wang, S. Kruk, K. Koshelev, I. Kravchenko, B. Luther-Davies, Y. Kivshar, *Nano Lett.* **2018**, *18*, 3978.
- [23] B. Reineke, B. Sain, R. Z. Zhao, L. Carletti, B. Y. Liu, L. L. Huang, C. De Angelis, T. Zentgraf, *Nano Lett.* **2019**, *19*, 6585.
- [24] G. Yang, Z. Li, Q. Kang, K. Guo, H. Zhang, Z. Guo, *J. Phys. D: Appl. Phys.* **2021**, *54*, 175110.
- [25] L. Huang, X. Chen, H. Muhlenbernd, H. Zhang, S. Chen, B. Bai, Q. Tan, G. Jin, K. W. Cheah, C. W. Qiu, J. Li, T. Zentgraf, S. Zhang, *Nat. Commun.* **2013**, *4*, 2808.
- [26] G. Zheng, H. Muhlenbernd, M. Kenney, G. Li, T. Zentgraf, S. Zhang, *Nat. Nanotechnol.* **2015**, *10*, 308.
- [27] X. Ding, Z. Wang, G. Hu, J. Liu, K. Zhang, H. Li, B. Ratni, S. N. Burokur, Q. Wu, J. Tan, *Photonix* **2020**, *1*, 16.
- [28] I. Kim, M. A. Ansari, M. Q. Mehmood, W. S. Kim, J. Jang, M. Zubair, Y. K. Kim, J. Rho, *Adv. Mater.* **2020**, *32*, 2004664.
- [29] E. Arbabi, S. M. Kamali, A. Arbabi, A. Faraon, *ACS Photonics* **2019**, *6*, 2712.
- [30] G. Yoon, D. Lee, K. T. Nam, J. Rho, *ACS Nano* **2018**, *12*, 6421.
- [31] J. Jang, H. Jeong, G. Hu, C. W. Qiu, K. T. Nam, J. Rho, *Adv. Opt. Mater.* **2019**, *7*, 1970016.
- [32] Y. Bao, Y. Yu, H. Xu, Q. Lin, Y. Wang, J. Li, Z. Zhou, X. Wang, *Adv. Funct. Mater.* **2018**, *28*, 1805306.
- [33] X. Luo, Y. Hu, X. Li, Y. Jiang, Y. Wang, P. Dai, Q. Liu, Z. Shu, H. Duan, *Adv. Opt. Mater.* **2020**, *8*, 1902020.
- [34] L. Huang, S. Zhang, T. Zentgraf, *Nanophotonics* **2018**, *7*, 1169.
- [35] J. Sung, G.-Y. Lee, B. Lee, *Nanophotonics* **2019**, *8*, 1701.
- [36] R. Zhao, L. Huang, Y. Wang, *Photonix* **2020**, *1*, 20.
- [37] B. Wang, F. Dong, Q.-T. Li, D. Yang, C. Sun, J. Chen, Z. Song, L. Xu, W. Chu, Y.-F. Xiao, *Nano Lett.* **2016**, *16*, 5235.
- [38] L. Jin, Z. Dong, S. Mei, Y. F. Yu, Z. Wei, Z. Pan, S. D. Rezaei, X. Li, A. I. Kuznetsov, Y. S. Kivshar, *Nano Lett.* **2018**, *18*, 8016.
- [39] D. Wen, F. Yue, G. Li, G. Zheng, K. Chan, S. Chen, M. Chen, K. F. Li, P. W. H. Wong, K. W. Cheah, *Nat. Commun.* **2015**, *6*, 8241.
- [40] J. B. Mueller, N. A. Rubin, R. C. Devlin, B. Groever, F. Capasso, *Phys. Rev. Lett.* **2017**, *118*, 113901.
- [41] Z. Deng, J. Deng, X. Zhuang, S. Wang, K. Li, Y. Wang, Y. Chi, X. Ye, J. Xu, G. Wang, *Nano Lett.* **2018**, *18*, 2885.
- [42] R. Zhao, B. Sain, Q. Wei, C. Tang, X. Li, T. Weiss, L. Huang, Y. Wang, T. Zentgraf, *Light: Sci. Appl.* **2018**, *7*, 95.
- [43] S. M. Kamali, E. Arbabi, A. Arbabi, Y. Horie, M. Faraji-Dana, A. Faraon, *Phys. Rev. X* **2017**, *7*, 041056.
- [44] E. Wang, J. Niu, Y. Liang, H. Li, Y. Hua, L. Shi, C. Xie, *Adv. Opt. Mater.* **2020**, *8*, 1901674.
- [45] X. Fang, H. Ren, M. Gu, *Nat. Photonics* **2020**, *14*, 102.
- [46] H. Zhou, B. Sain, Y. Wang, C. Schlickriede, R. Zhao, X. Zhang, Q. Wei, X. Li, L. Huang, T. Zentgraf, *ACS Nano* **2020**, *14*, 5553.
- [47] K. Chen, G. Ding, G. Hu, Z. Jin, J. Zhao, Y. Feng, T. Jiang, A. Alù, C. W. Qiu, *Adv. Mater.* **2020**, *32*, 1906352.
- [48] D. Frese, Q. Wei, Y. Wang, L. Huang, T. Zentgraf, *Nano Lett.* **2019**, *19*, 3976.
- [49] K. T. Lim, H. Liu, Y. Liu, J. K. Yang, *Nat. Commun.* **2019**, *10*, 25.
- [50] Q. Wei, B. Sain, Y. Wang, B. Reineke, X. Li, L. Huang, T. Zentgraf, *Nano Lett.* **2019**, *19*, 8964.
- [51] Y. Hu, X. Luo, Y. Chen, Q. Liu, X. Li, Y. Wang, N. Liu, H. Duan, *Light: Sci. Appl.* **2019**, *8*, 86.
- [52] Q. Song, S. Khadir, S. Vézian, B. Damianno, P. de Mierry, S. Chenot, V. Brandli, R. Laberdesque, B. Wattellier, P. Genevet, *Nanophotonics* **2020**, *10*, 697.
- [53] N. Mao, J. Deng, X. Zhang, Y. Tang, M. Jin, Y. Li, X. Liu, K. Li, T. Cao, K. Cheah, H. Wang, J. Ng, G. Li, *Nano Lett.* **2020**, *20*, 7463.
- [54] E. Schonbrun, K. Seo, K. B. Crozier, *Nano Lett.* **2011**, *11*, 4299.
- [55] K. Bi, Q. Wang, J. Xu, L. Chen, C. Lan, M. Lei, *Adv. Opt. Mater.* **2021**, *9*, 2001474.
- [56] P. Xie, Z. Zhang, Z. Wang, K. Sun, R. Fan, *Research* **2019**, *2019*, 1021368.
- [57] J. Gao, Y. Zhang, Y. Sun, Q. Wu, *Results Phys.* **2020**, *17*, 103038.
- [58] Z. X. Wang, J. W. Wu, L. W. Wu, Y. Gou, H. F. Ma, Q. Cheng, T. J. Cui, *Adv. Opt. Mater.* **2020**, *9*, 2001609.